Misfit dislocation structure and thermal boundary conductance of GaN/AIN interfaces



Cite as: J. Appl. Phys. **130**, 035301 (2021); https://doi.org/10.1063/5.0049662 Submitted: 07 March 2021 • Accepted: 01 June 2021 • Published Online: 15 July 2021

🗓 Jiaqi Sun, Yang Li, 🗓 Yenal Karaaslan, et al.

COLLECTIONS

F This paper was selected as Featured







ARTICLES YOU MAY BE INTERESTED IN

Interfacial engineering for the enhancement of interfacial thermal conductance in GaN/AIN heterostructure

Journal of Applied Physics 129, 235102 (2021); https://doi.org/10.1063/5.0052742

Atomistic origin of compositional pulling effect in wurtzite (B, Al, $In)_XGa_{1-X}N$: A first-principles study

Journal of Applied Physics 130, 035704 (2021); https://doi.org/10.1063/5.0050102

An improved design for e-mode AlGaN/GaN HEMT with gate stack β -Ga₂O₃/p-GaN structure Journal of Applied Physics 130, 035703 (2021); https://doi.org/10.1063/5.0051274





Misfit dislocation structure and thermal boundary conductance of GaN/AIN interfaces •

Cite as: J. Appl. Phys. 130, 035301 (2021); doi: 10.1063/5.0049662

Submitted: 7 March 2021 · Accepted: 1 June 2021 ·

Published Online: 15 July 2021







Jiaqi Sun,^{1,a)} 📵 Yang Li,¹ Yenal Karaaslan,² 📵 Cem Sevik,^{2,3} 📵 and Youping Chen¹ 📵

AFFILIATIONS

- Department of Mechanical and Aerospace Engineering, University of Florida, Gainesville, Florida 26555, USA
- ²Department of Mechanical Engineering, Eskisehir Technical University, Eskişehir, Turkey
- ³Department of Physics, University of Antwerp, Groenenborgerlaan 171, 2020 Antwerp, Belgium

ABSTRACT

The structure and thermal boundary conductance of the wurtzite GaN/AlN (0001) interface are investigated using molecular dynamics simulation. Simulation results with three different empirical interatomic potentials have produced similar misfit dislocation networks and dislocation core structures. Specifically, the misfit dislocation network at the GaN/AlN interface is found to consist of pure edge dislocations with a Burgers vector of $1/3\langle 1\bar{2}10\rangle$ and the misfit dislocation core has an eight-atom ring structure. Although different interatomic potentials lead to different dislocation properties and thermal conductance values, all have demonstrated a significant effect of misfit dislocations on the thermal boundary conductance of the GaN/AlN (0001) interface.

Published under an exclusive license by AIP Publishing. https://doi.org/10.1063/5.0049662

I. INTRODUCTION

Semiconductor devices such as electronic and photonic devices are heterogeneous structures built from two or more different materials. The interface(s) between different materials in the heterostructures plays an essential role in the device action. A high density of defects is often observed accompanying the interfaces, influencing the performance of the devices. These defects form during the fabrication processes. Currently, the main bottom-up method used today for fabrication of semiconductor heterostructures is heteroepitaxy, such as molecular beam epitaxy and metal organic chemical vapor deposition. It is theoretically understood that lattice-mismatched heterostructures accommodate misfit strains by elastic deformation when the epilayer is thin and by the formation of misfit dislocations when the epilayer thickness exceeds a critical value, known as the critical thickness, usually a few nanometers.^{2,3} Regardless of the growth mechanisms or conditions, increasing the epilayer thickness will ultimately lead to the formation of misfit dislocations and concomitant threading dislocations.4

Another method to fabricate semiconductor heterostructures is direct wafer bonding. Recent developments in surface-activated bonding make direct bonding an important alternative tool for heterogeneous integration. Various semiconductor wafers have been bonded directly at room temperature on atomically clean surfaces created by ion beam bombardment. For example, gallium nitride (GaN) has been directly bonded to Si,⁵ SiC,^{6–8} GaAs,⁹ and diamond¹⁰ using the surface-activated bonding method. HRTEM (high-resolution transmission electron microscopy) images show that there are misfit dislocations formed at the interface to accommodate lattice mismatch⁶ and that heterostructures with atomically flat interfaces can be realized. The advantage of this direct bonding technique is that it can avoid the usual high-density threading dislocations in the epilayers, and consequently the heterostructure has misfit dislocations as the only type of defects resulting from the fabrication process.^{6,7}

Interface misfit dislocations are thus the most important defects in semiconductor heterostructures as they are unavoidable in lattice-mismatched heterointerfaces, directly affect the electronic properties of the devices, ^{11,12} and determine the ultimate limit of the performance of the heterostructure. Moreover, interfaces and defects scatter phonons, leading to localized heating that severely limit the performance and reliability of the devices. For example, the peak power density in GaN high-electron-mobility transistors is strongly limited by self-heating in the devices. The localized heating at the interfaces can limit reliable output power to only 1/8th of the reported maximums. ¹³

a)Author to whom correspondence should be addressed: sunjiagi@ufl.edu

The GaN/AlN interface is an important interface in GaN high-electron-mobility transistors. GaN/AlN quantum wells and quantum dots are also widely used in optoelectronic devices. 14-16 In addition, GaN and AlN are important third generation semiconductor materials that have wide bandgaps of 3.4 and 6.2 eV, respectively. Their heterostructures have strong spontaneous polarization and piezoelectric polarization, as a result of the lattice-mismatched heterointerface. The piezoelectric properties, as well as the optoelectronic properties, can also be significantly affected by the defects and localized heating at the interfaces. Our understanding of the defect structure and the effect of the defects on self-heating, however, is limited, as current research efforts to understand thermal transport properties across heterointerfaces 17,18 have so far mainly focused on coherent interfaces that are free of misfit dislocations. For example, the phonon thermal conductance of GaN/AlN interface was recently calculated by Polanco and Lindsay using a nonequilibrium Green's function formalism in the harmonic limit with interfacial interatomic force constants (IFCs) obtained from density functional theory (DFT) calculations; ¹⁷ in their model, the GaN/AlN interface was assumed to be coherent, where AlN is strained to match the lattice of GaN.

The objective of this work is to investigate the misfit dislocation structure and the effect on the thermal boundary conductance of the wurtzite GaN/AlN (0001) interface using molecular dynamics (MD) simulation. We employ three different interatomic potentials to describe the atomic interaction in the systems: (1) the Stillinger–Weber (SW) potential for GaN/AlN developed by Zhou et al., ¹⁹ (2) a potential based on the mixing rule and the AlN potential developed by Tungare et al. ²⁰ combined with the GaN potential developed by Nord et al., ²¹ and (3) the transferable Tersoff-type potential for group-III nitrides developed by Karaaslan et al. ²²

The paper is organized as follows. After the Introduction, the methodology, including details of the interatomic potentials and the simulation setups, is introduced in Sec. II. Section III presents the multiscale structures of the wurtzite GaN and AlN (0001) interfaces obtained from MD simulations of the direct bonding process, including the misfit dislocation network at the interface and the atomic-scale dislocation core structure. Simulation results of the Peierls stress of the misfit dislocations and the interface reaction to phonon wave packets are also included in Sec. III. Section IV presents the simulation results of the thermal boundary conductance of semi-coherent GaN/AlN interfaces and the comparison with that of coherent interfaces. The effects of the specimen size and temperature on the thermal boundary conductance are also included in Sec. IV. Major conclusions are summarized in Sec. V.

II. METHDOLOGY

A. Interatomic potentials

All the simulations reported in this work are performed using the large-scale atomic/molecular massively parallel simulator (LAMMPS) software. We employ the following three empirical interatomic potentials for the simulations:

(1) The Stillinger-Weber potential for GaN and AlN developed by Zhou et al.¹⁹ This potential built on the SW potential for GaN

TABLE I. SW potential parameters for AIN/GaN. 19

Parameters	Ga-Ga	Ga-N	N-N	N-Al	Al–Al	Al-Ga
ϵ (eV)	1.2000	2.1700	1.2000	2.2614	0.5650	0.5223
$\sigma(\mathring{\mathrm{A}})$	2.1000	1.6950	1.3000	1.7103	2.6674	2.7322
α	1.600	1.800	1.80	1.80	1.55	1.55
λ	32.5	32.5	32.5	32.5	0.0	0.0
γ	1.2	1.2	1.2	1.2	1.2	1.2
A	7.9170	7.9170	7.9170	7.9170	17.8118	17.8118
В	0.72	0.72	0.72	0.72	0.72	0.72

developed by Béré and Serra,²³ the parameters of which were fitted to the experimental results of elastic constants and lattice constant (a = 3.19 Å, c = 5.21 Å for GaN and a = 3.09 Å, c = 5.03 Å for AlN). Since the parameters σ and ϵ of the SW potential are proportional to their lattice constant and cohesive energy, respectively, Zhou and co-workers¹⁹ obtained the parameters σ and ϵ of Al–Al and Al–Ga interactions by rescaling the Ga-Ga interaction according to the experimental values of lattice constant and cohesive energy. The Al-N interaction is fitted to the experimental lattice constant and cohesive energy of wurtzite AlN.²⁴ The parameters of this GaN/AlN potential are presented in Table I. This potential has been applied to simulation of thermal boundary conductance of GaN/Al²⁵ and the growth of GaN on AlN.²⁶ It has also been used by Li et al. to investigate the structure of the GaN/AlN heterointerface and the deformation mechanism.2

- (2) A Tersoff potential developed based on the mixing rule. Mixing rule is an empirical method to generate interatomic potentials of a multicomponent system from the respective single element interaction.²⁸ In this work, we use the mixing rule to construct a potential for the GaN/AlN system based on the AlN potential developed by Tungare et al.²⁰ and the GaN potential developed by Nord et al. 21 The AlN potential by Tungare et al.²⁰ was obtained by adjusting an existing zinc blende AlN potential to fit the properties of wurtzite AlN. The optimized potential was tested in terms of lattice constants (a = 3.112 Å, c = 4.9823 Å), bulk modulus, cohesive energy, and thermal expansion, in good agreement with experimental values. The GaN potential by Nord et al.21 was obtained by fitting to density functional theory (DFT) calculations and experimental measured values of lattice constants (a = 3.18 Å, c = 5.193 Å), cohesive energy, and elastic constants. This potential has been shown to reproduce point defect properties, melting behavior, and nitrogen solubility, in good agreement with DFT calculations. The two potentials together provide the Al-Al, Al-N, N-N, N-Ga, and Ga-Ga interactions. Therefore, in this work, we only need to obtain the Al-Ga interaction using the mixing rule. The potential parameters are presented
- (3) The transferable Tersoff-type potential developed by Karaaslan and co-workers for group-III nitrides.²² This potential was obtained through an optimization procedure based on particle swarms optimization. The parameters of the hexagonal monolayer and zinc blende structure BN, AlN, and GaN were

TABLE II. Mixing rule-based Tersoff potential parameters for AIN/GaN.

Parameters	Ga-Ga	Ga-N	N-N	N-Al	Al-Al	Al-Ga
A(eV)	535.199	6136.44	1044.77	1847.752	492.6746	513.4968
B(eV)	410.132	3864.27	423.769	257.3159	23.029 55	97.1862
γ	0.7874	0.001 632	0.7761	0.000 001 1	0.3168	0.3168
$\lambda_1(1/\text{Å})$	1.609 16	2.935 16	3.557 87	3.213 10	2.585 22	2.097 19
$\lambda_2(1/\text{Å})$	1.449 70	2.639 06	2.384 26	1.860 59	0.9274	1.188 57
$R(\mathring{\mathbf{A}})$	2.87	2.90	2.20	2.34	2.70	2.785
$D(\mathring{\mathrm{A}})$	0.15	0.20	0.20	0.15	0.10	0.125
$\lambda_3(1/\text{Å})$	1.846	0	0	0	1.5	1.673
c	1.918	65.207	0.1785	100 390	0.0748	0.0748
d	0.75	2.821 00	0.20172	16.207	19.5691	19.5691

optimized simultaneously to fitting to first-principles calculations of lattice constants (a = 3.503 Å, c = 5.720 Å for GaN and a = 3.381 Å, c = 5.521 Å for AlN), equation of states, phonon frequencies, defect energies, and the difference of formation energies per atom of single-layer h and bulk zinc blende crystal phases. It is noted that this potential is the only one that was fitted to phonon frequencies of AlN and GaN. The predicted thermal properties as well as the structural, mechanical, and vibrational properties of all materials are in good agreement with existing experimental and first-principles data. In particular, this Tersoff-type potential has been tested in reproducing phonon dispersion relations and lattice thermal transport properties of both zinc blende and wurtzite structures of AlN and GaN. The potential parameters are listed in Table III.

B. Computer models and simulation setups

The wurtzite GaN/AlN (0001) heterointerface can have either Al–N bonds or Ga–N bonds at the interface. We have calculated the interfacial energy of the two types of interfaces by calculating the difference between the total potential energy of the heterostructure and the sum of the bulk potential energies of the GaN and

AlN crystals. Calculation results with all three interatomic potentials show that the Al–N bonded interface has lower interface energy than the Ga–N bonded interface. Therefore, in this work, we focus on the GaN/AlN (0001) heterostructure that has the Al–N bonds at the interface. This is consistent with existing simulation results that the Al–N bonded interface is energetically more favorable, ²⁹ while the thermal boundary resistances is very close to that of the interface that has the Ga–N bonds. ¹⁷

The dislocation structure of the GaN/AlN (0001) interface is obtained through simulations of the direct wafer bonding process. This process consists of two steps. In step 1, two single crystals are put into contact through pressure applied to the surfaces of the two crystals at room temperature to initiate the bonding. In step 2, the bonded heterostructure is annealed at high temperature $(600-1000\,^{\circ}\mathrm{C})$.

Our simulations for the dislocation structure follow these two steps. First, we simulate the single crystals AlN and GaN using the three potentials, respectively. The MD simulations are shown to reproduce the exact structures and lattice constants of GaN and AlN that the interatomic potentials were fitted to. The well-equilibrated GaN and AlN single crystals are then placed in one computer model, where the GaN and AlN single crystals are put

TABLE III. Tersoff-type potential parameters for GaN and AlN by Karaaslan et al.²² and for GaN/AlN.

Parameters	Ga-N-N	N-Ga-Ga	Al-N-N	N-Al-Al	N-Ga-Al	N-Al-Ga
A(eV)	2 249.391 746	2 249.391 746	1 258.567 263	1 258.567 263	2 249.391 746	1 258.567 263
B(eV)	764.751 142	764.751 142	453.228 512	453.228 512	764.751 142	453.228 512
γ	1	1	1	1	1	1
$\lambda_1(1/\text{Å})$	2.652 624	2.652 624	2.434 869	2.434 869	2.652 624	2.434 869
$\lambda_2(1/\text{Å})$	1.963 739	1.963 739	1.717 680	1.717 680	1.963 739	1.717 680
$R(\mathring{A})$	2.65	2.65	2.55	2.55	2.70	2.70
$D(\mathring{\mathrm{A}})$	0.15	0.15	0.15	0.15	0.20	0.20
$\lambda_3(1/\text{Å})$	1.453 060	1.166 408	1.186 759	1.100 709	3.363 107	3.363 107
c	45 996.528 912	44 736.208 668	19 110.741 778	27 568.039 128	45 896.229 303	45 896.229 303
d	13.083 985	12.497 037	10.882 090	8.292 436	14.231 385	14.231 385
h	$-0.990\ 019$	-0.693793	-0.972662	-0.816226	-0.836813	-0.836813
n	0.761 872	1.070 552	0.598 233	1.220 882	5.569 371	5.569 371
$\beta (\times 10^{-6})$	2.143 554	2.642 801	2.133 047	2.496 023	1.829 919	1.829 919

into contact at the (0001) surface by applying pressure $P=150\,\mathrm{bar}$ on the top surfaces of the GaN crystal at the [0001] direction for 10 ps at 300 K temperature using the NPT ensemble with a Nosé–Hoover thermostat. Periodic boundary conditions are used in the lateral directions of the AlN crystal, which serves as the substrate. The time step is set to 1 fs.

In step 2, a series of finite-temperature simulations of the annealing process is performed. This process starts at T = 1000 K for 50 ps; the GaN/AlN heterostructure is then relaxed with a decreased temperature at 600, 300, 10, and 0.1 K for 10 ps each. The final heterostructure obtained in the MD simulation using the mixing rule-based Tersoff potential is found to be fully relaxed. The structural results, including the dislocation network and dislocation core structure, are found to be identical to the simulation results using the initial structure that is built based on the concept of coincidence site lattice (CSL) with periodic boundary conditions for both GaN and AlN. According to the concept of CSL, the minimum energy configuration of the heterostructure is the one with minimum coincidence sites per area. For the mixing rulebased Tersoff potential with the lattice mismatch of 2.18% between GaN and AlN, the smallest interface that has minimum energy density contains 46 by 46 GaN unit cells and 47 by 47 AlN unit cells along the [0110] direction. Since the SW potential by Zhou et al. 19 and the Tersoff-type potential by Karaaslan et al. 22 can only be used for simulation cells with periodic boundary conditions, the computer models for the structural simulations with these two potentials are thus built to have the minimum CSL per interface area. These simulations still follow the two steps, i.e., equilibration in the NPT ensemble with Nosé-Hoover thermostat, with temperature $T=300\,\mathrm{K}$ and pressure $P=150\,\mathrm{bar},$ followed by a series of NPT simulations of annealing with $T=1000,\,600,\,300,\,10,\,$ and $0.1\,\mathrm{K}.$

The obtained structures are then used to simulate the heat flow process using the direct heat source-heat sink method, 30 as shown in Figs. 1(a)-1(c), with each interface containing two misfit dislocations and the smallest length of the specimens is 105 nm. For comparison, we also build strained heterostructures with coherent interfaces. This is achieved by using a small cross-sectional area that contains only 4 by 4 unit cells of GaN and AlN, respectively, with period boundary conditions (PBCs) being applied in the lateral directions of the heterostructure, as shown in Fig. 1(b). With such a small cross-sectional area constrained by PBCs, the computer models are free of dislocations, as the smallest interface that has one misfit dislocation contains 46 by 46 GaN unit cells and 47 by 47 AlN unit cells, as required by the mixing rule-based potentials. Computer models with such small cross-sectional areas and PBCs are not physical. Nevertheless, simulation results of such structures can be used to quantify the role of misfit dislocations on thermal transport properties such as thermal boundary

After the equilibration, the boundaries of the computer model are then fixed in the direction of the specimen length. A small region in the AlN crystal is heated to simulate a heat source, while another region on the GaN crystal is cooled to act as a heat sink. These two regions have the same dimension, and the energy added and removed at each time step are identical. Therefore, a steady-state heat flow can be generated in the heterostructure through this process.

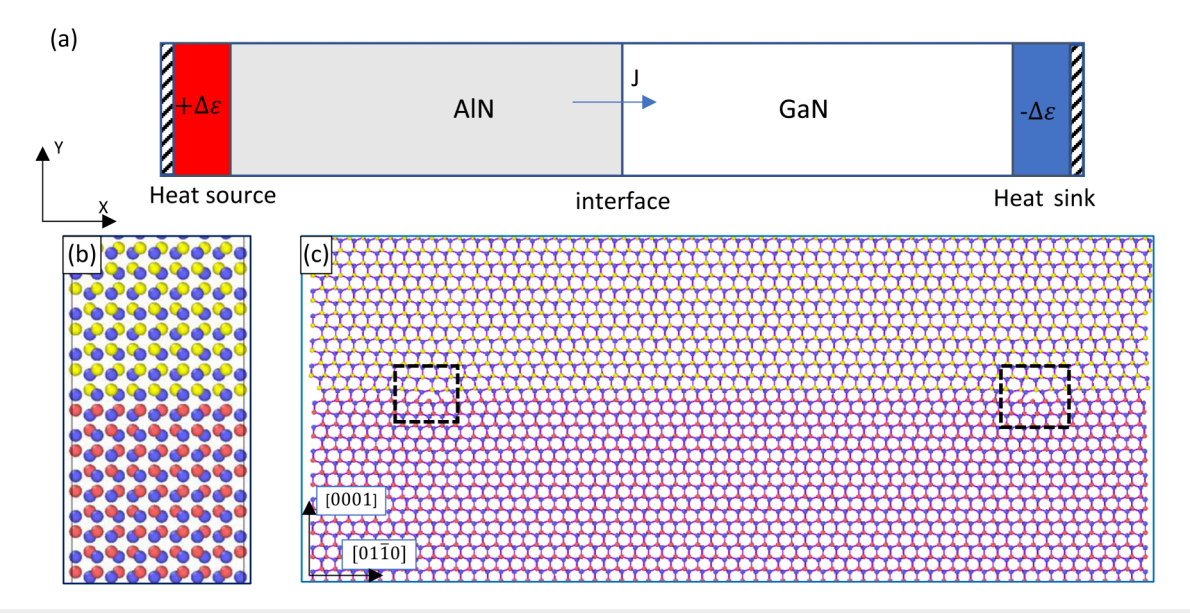


FIG. 1. (a) Top view of the computer model for simulation of steady-state heat flow to measure the thermal boundary conductance; the energy added to the heat source and the energy removed from the heat sink are identical; (b) cross-sectional view of the coherent interface that contains 4 by 4 GaN and AlN unit cells; (c) cross-sectional view of the semi-coherent interface that contains two misfit dislocations; the dotted frames highlight the two misfit dislocations. The red, blue, and yellow atoms represent Al, N, and Ga atoms, respectively.

After the system reaches steady state, the temperature profile is recorded every 50 ps and averaged over 5 ps for a total simulation time of 4 ns. Based on the temperature profile, the temperature jump ΔT can be estimated, and the thermal conductance G_k can then be calculated by

$$J = G_k \Delta T, \tag{1}$$

where J is the heat flux, which is given by

$$J = \frac{\Delta \varepsilon}{A \cdot \Delta t}.$$
 (2)

III. DISLOCATION STRUCTURE AT THE GaN/AIN (0001) INTERFACE

The equilibrium structures of the wurtzite GaN/AlN (0001) interface that has Al–N bonds at the interface are obtained through simulations of the direct bonding process of GaN and AlN single crystals. Figure 2 presents the simulation results of the misfit dislocation network at the interface, viewed using the dislocation extraction algorithm (DXA) analysis, ³¹ obtained from simulations with three different interatomic potentials. As can be seen from Fig. 2, a hexagonal-shaped network of the misfit dislocations has formed in the simulation using each of the three interatomic potentials. The misfit dislocation spacing is 9.89 nm for SW potential, 14.66 nm for the mixing rule-based Tersoff potential, and 9.81 nm for the transferrable Tersoff potential for group-III nitrides. Misfit dislocations are found to consist of pure edge dislocations with a Burgers vector of $1/3\langle1\bar{2}10\rangle$.

Figure 3 presents a zoomed-in view of the potential energy contour of the GaN and AlN layers at the interface. Different color bars are used here for the purpose of an optimum visualization. Hexagonal misfit dislocation network can again be discerned due to the energetic difference between atoms in the coherent region and atoms near the dislocations. Atomic-scale defects such as vacancy or crack-like structures can be observed on the GaN layer. By contrast, the AlN layer is free from defects for all three potentials. In addition, the GaN atoms are found to have higher potential energy than the AlN atoms.

A calculation of the deformation of the unit cells shows that the GaN unit cells undergo tensile deformation, while the AlN unit cells are under compression. Specifically, for the SW potential, the GaN unit cells at the coherent regions of the interface experience a tensile strain of 2.16% in the basal plane, while the AlN unit cells undergo a compressive strain of 0.87%. For the mixing rule-based Tersoff potentials, it is 1.51% tensile strain for GaN but 0.87% compressive strain for AlN. For the Tersoff-type potential for group-III nitrides, it is 2.33% tensile strain for GaN but 1.36% compressive strain for AlN. All three simulation results indicate that the GaN layer undergoes larger deformation than the AlN layer, suggesting that AlN has a higher resistance to deformation. This is consistent with the experimental and density functional theory calculation results that AlN possesses higher hardness (17.2 GPa) than GaN (10.5 GPa)³³ and also higher bonding energy (2.74 eV) than GaN $(2.45 \text{ eV}).^{34}$

In Fig. 4, we present a cross-sectional view of the atomic positions near a misfit dislocation at the GaN/AlN interface, obtained from simulations using different potentials. As can be seen from Fig. 4, the dislocation core has the structure of an eight-atom ring, where a total of eight atoms surround the dislocation line with one atom as an immobilized radical. This eight-atom ring structure of misfit dislocations is obtained in the simulations of all three potentials and is found to be consistent with the MD simulation results of dislocations in GaN single crystals by Béré and Serra 23 and Termentzidis *et al.*, 35 as well as the experimental result by Yoo *et al.*, 36 as shown in the inset of Fig. 4(c).

To investigate the mobility of the misfit dislocations, a series of MD simulations is performed to measure the Peierls stress of the misfit dislocations. Peierls stress is a fundamental property of dislocations and is defined as the minimum shear stress required to move a dislocation in a crystal. To measure the Peierls stress, an incrementally increased shear force is applied on the top and bottom layers of a well-equilibrated GaN/AlN heterostructure. The direction of the shear force is parallel to the Burgers vector, i.e., the $[01\bar{1}0]$ direction. The simulations are performed for computer models at 0.1 K temperature. The movements of the dislocations are monitored via DXA³¹ in OVITO. The dislocations begin to move, the Peierls stress is calculated from the applied force and the cross-sectional area at that time.

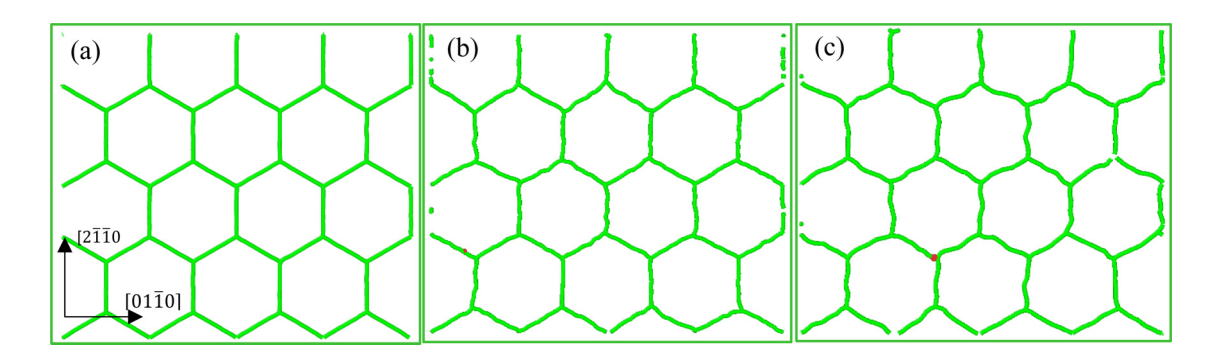


FIG. 2. Misfit dislocation network at the GaN/AIN interface represented via the dislocation extraction algorithm (DXA)³¹ in OVITO,³² obtained from (a) the SW potential, (b) the mixing rule-based Tersoff potentials, and (c) the transferable Tersoff potential for group-III nitrides.

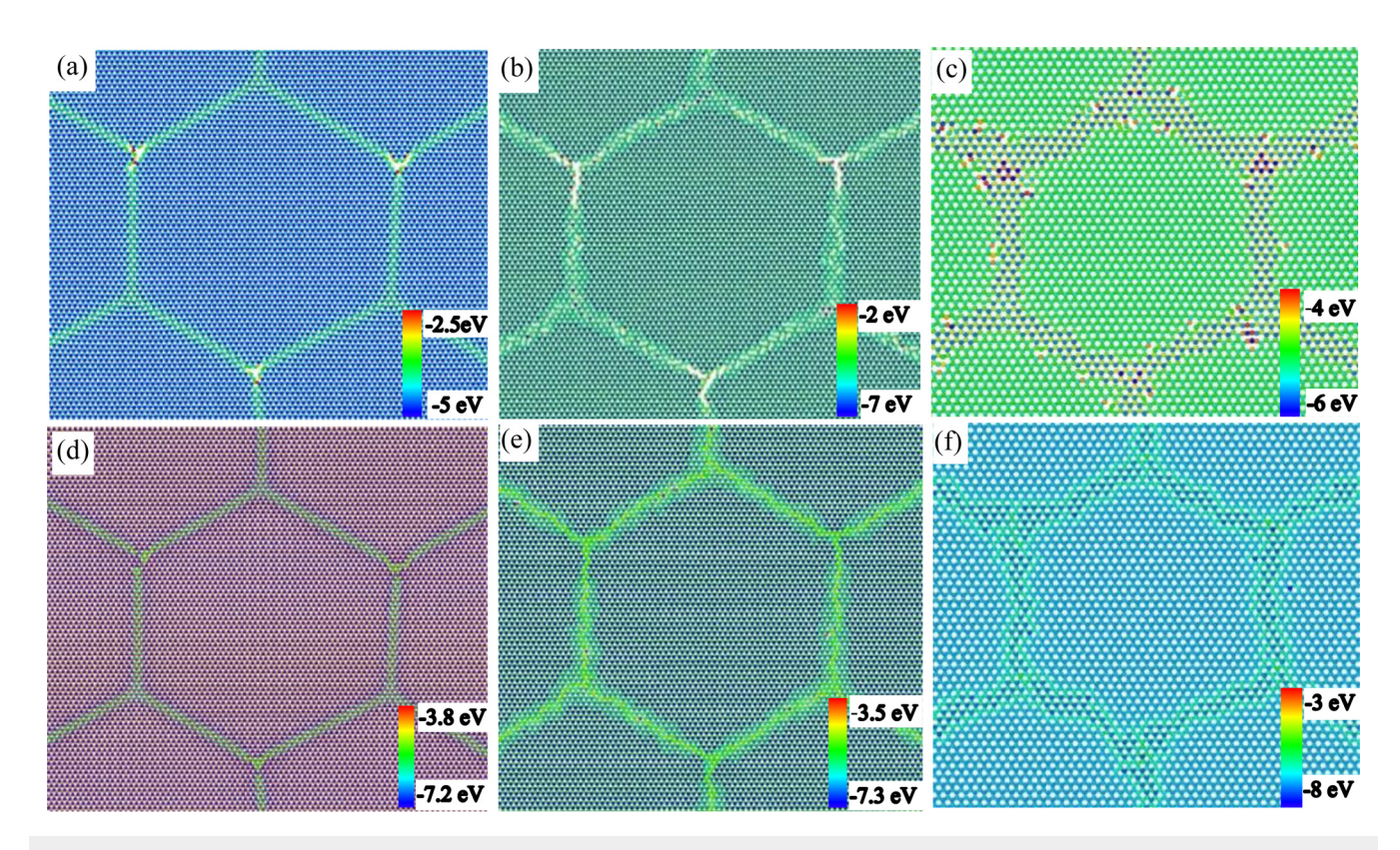


FIG. 3. Potential energy of GaN [(a)–(c)] and AlN [(d)–(f)] atoms in a single hexagonal unit in the misfit dislocation network at the GaN/AlN (0001) interface, obtained in MD simulation with the SW potential [(a) and (d)], the mixing rule-based Tersoff potential [(b) and (e)], and the transferable Tersoff potential for group-III nitrides [(c) and (f)].

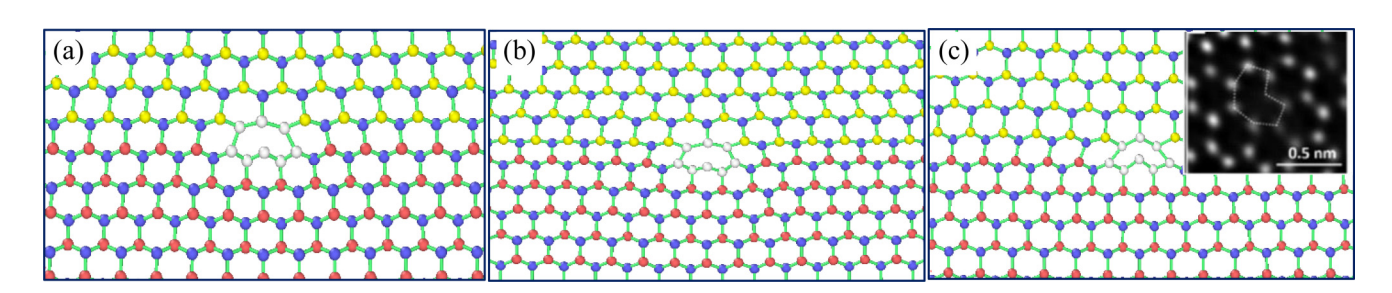
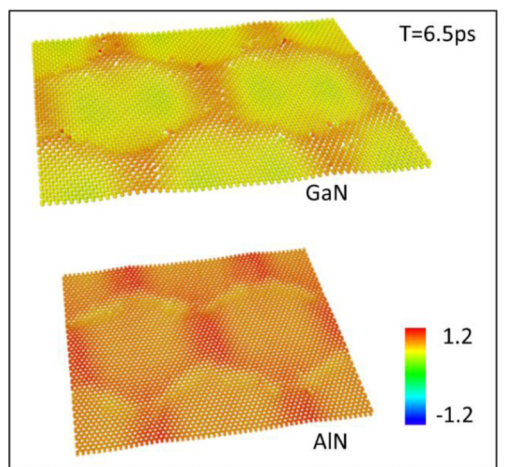


FIG. 4. The dislocation core structure obtained by using (a) the SW potential, (b) the mixing rule-based Tersoff potential, and (c) the transferable Tersoff potential for group-III nitrides. Here, Al atoms are colored with red, N atoms with blue, and Ga atoms with yellow; the atoms colored by white are atoms that form the dislocation core; the inset in (c) is a STEM image of a GaN single crystal by Yoo *et al.*, ³⁶ showing a dislocation core with an eight-atom ring structure, and is reproduced with permission from Yoo *et al.*, Appl. Phys. Lett. **112**, 131901 (2018). Copyright 2018 AIP Publishing LLC.

TABLE IV. Peierls stress for GaN/AIN interface misfit dislocations.

	Peierls stress (GPa)
SW ¹⁹	0.956
Mixing rule-based Tersoff ^{20,21}	9.69
Transferrable Tersoff ²²	9.85

Table IV presents the results of Peierls stress measured from simulations using the three potentials. As can been seen from Table IV, the values of Peierls stress produced by the mixing rule-based Tersoff potential and the transferrable Tersoff potential is very large, indicating that the mobility of the misfit dislocations is very low and the misfit dislocations are essentially sessile. The SW potential, by contrast, gives a much lower Peierls stress, which



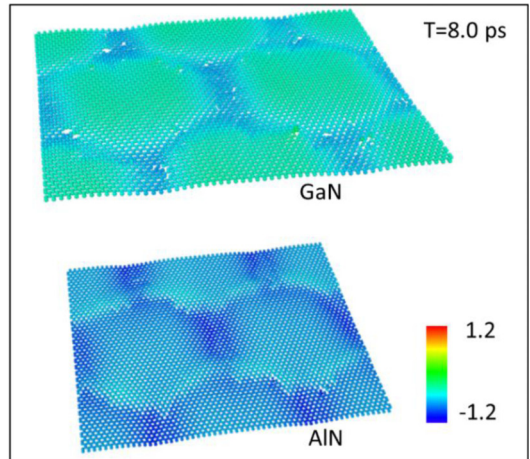


FIG. 5. 3D scatterplots of the displacements of the GaN atoms and AlN layers at the GaN/AlN interface at simulation time t = 6.5 and 8.0 ps, respectively. The unit of the color bar is the amplitude of the incident wave packet, which is 0.001 Å. The red color in the atomic displacements in the left figure and the blue color in the right represent two opposite displacement directions, showing that the dislocations and atoms near the dislocations are vibrating in phase.

implies that the dislocations produced by this potential possess higher mobility.

Visualizations of the transient processes of misfit dislocations' reaction to applied stress have shown that the misfit dislocations are most stable in simulations with the transferrable Tersoff potential. In addition, the misfit dislocations move collectively under stress in simulations with the transferrable Tersoff potential, while there are vibrations of individual atoms in the dislocation networks in simulations with the other two potentials.

To provide more details on the vibrations of the misfit dislocations, a wave packet simulation is performed using the transferrable Tersoff potential for visualization of the reaction of the misfit dislocations to an ultrashort heat pulse. The heat pulse is constructed using the phonon wave packet technique developed by Schelling and co-workers for MD simulation, 37,38 based on the phonon dispersion relation of the AlN. The wave packet has a central frequency of 1.5 THz and a wavelength of 8 nm. The computer model of the GaN/AlN heterostructure has a total length of 300 nm, and the structure, including the misfit dislocation network and the dislocation core structure, is obtained following the procedure outlined in Sec. II. Thereafter, the computer model is cooled down to 10^{-5} K. The displacements of the atoms at the interface are recorded in the simulation as the phonon pulse propagates across the interface. In Fig. 5, we present 3D scatterplots for the displacements of the GaN and AlN layers at the GaN/AlN interface. As can be seen from Fig. 5, the misfit dislocations and the atoms near the dislocations vibrate in phase, indicating no resonance between the misfit dislocation network and the phonon wave packet. However, the vibration amplitude of the dislocations is 20% larger than the amplitude of the incident wave packet.

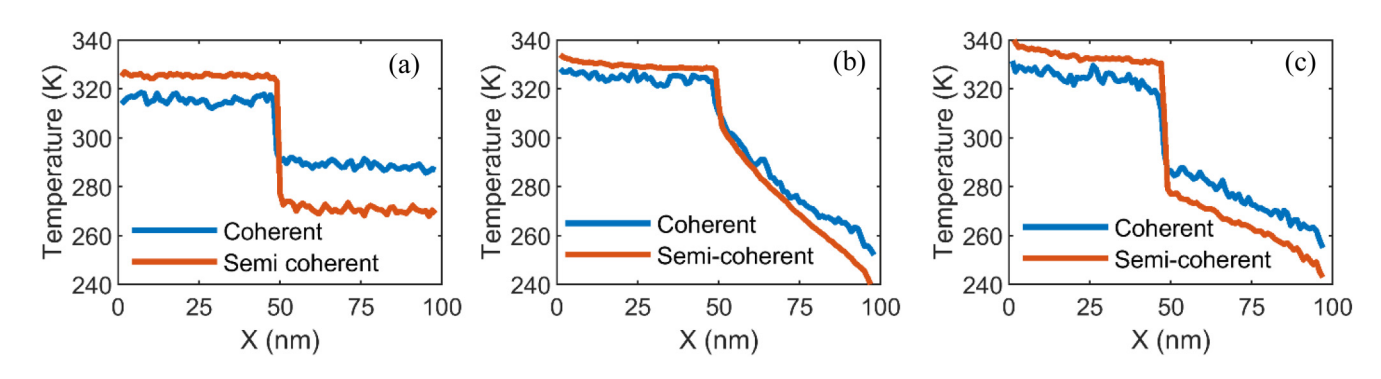


FIG. 6. Temperature profile of GaN/AIN heterostructures using (a) the SW potential, (b) the mixing rule-based Tersoff potential, and (c) the transferable Tersoff potential for group-III nitrides. Applied heat flux are 2.9, 5.7, and 9.7 GW/m², respectively.

TABLE V. Thermal conductance values of the GaN/AIN interface.

	Coherent interface (GW/m ² K)	Semi-coherent interface (GW/m ² K)	% of reduction
SW ¹⁹ Mixing rule-based Tersoff ^{20,21}	0.937 3.124	0.496 2.44	47.1% 21.9%
Transferrable Tersoff ²²	3.225	1.933	40.1%

IV. THERMAL BOUNDARY CONDUCTANCE

Interface thermal boundary resistance is usually manifested as a temperature drop at the interface. The inverse of this resistance is the thermal boundary conductance, which is defined as the ratio between applied heat flux and the resulting temperature drop at the interface. In this work, thermal boundary conductance of wurtzite GaN/AlN (0001) interfaces is measured in MD simulations of steady-state heat flow, using the direct heat source-heat sink method. The simulation results of the temperature profile, using the three different potentials, are presented in Fig. 5, in which the X axis represents the position along the direction of the heat flow. Each curve contains 100 data points located between the heat source and the heat sink, with the heat source and heat sink regions being excluded from the measurements. A temperature discontinuity can be observed in Fig. 6 at the interface location in simulations with all three potentials for both coherent and semi-coherent interfaces. The applied heat flux is adjusted for each model to ensure that the three computer models have a similar temperature while the temperature drop remains in the realistic range (20-80 K). Based on the obtained temperature drop and the input heat flux, the thermal boundary conductance of the GaN/AlN interface can be estimated. The results are summarized

in Table V. As can be seen from Table V, while different potentials lead to different thermal boundary conductance values, all three potentials predict a significant effect of misfit dislocations on the reduction of the thermal boundary conductance. The reductions are 47.1%, 21.9%, and 40.1% for the SW potential, the mixing rule-based potential, and the transferrable Tersoff-type potential, respectively.

Figure 7 presents the simulation results of the thermal boundary conductance as a function of applied heat flux, background temperature, and the length of the specimen in the direction of heat flow using the transferable Tersoff-type potential developed by Karaaslan et al. 22 As can be seen from Fig. 7(a), the thermal boundary conductance for both coherent and semi-coherent GaN/AlN interfaces do not change appreciably with applied heat flux. This means that the thermal boundary conductance is not a function of applied heat flux or temperature gradient, and hence the linear relation between heat flux and temperature drop is valid for the atomically flat GaN/AlN (0001) interfaces. Figure 7(b) presents the thermal conductance measured in the simulations with different average background temperature of the entire specimen. It is seen from Fig. 7(b) that the thermal boundary conductance for both coherent interface and semi-coherent interfaces increases significantly with the temperature. Such a strong temperature effect is consistent with the MD simulation results of the temperature effect on the thermal boundary conductance of the Al-GaN interface² and the Si-Ge interface.³⁹ To investigate the effect of specimen size on thermal boundary conductance, we have simulated three specimens that have specimen length 105, 150, and 200 nm, respectively. As can be seen from Fig. 7(c), the thermal boundary conductance for both coherent and semi-coherent interfaces increases with the specimen length.

It is noted that, among the three interatomic potentials, the transferable Tersoff potential is found to be the most efficient potential. It is 52% faster than mixing rule-based Tersoff potential and 96% faster than SW potential in the simulation of the thermal conductivity experiment, i.e., the direct heat source-heat sink method.

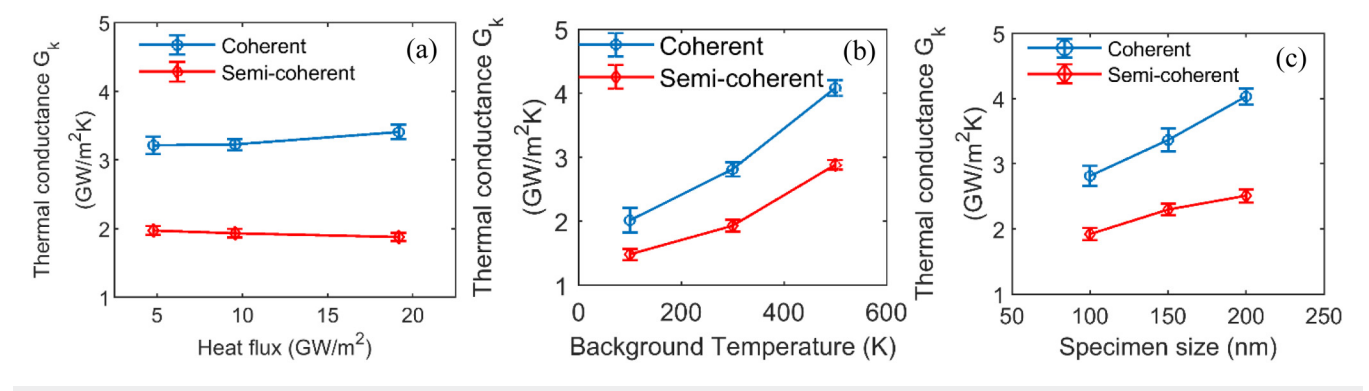


FIG. 7. Thermal conductance as a function of (a) applied heat flux, (b) average background temperature, and (c) the specimen length in the heat flow direction, obtained from MD simulations using the transferable Tersoff potential for group-III nitrides.

V. SUMMARY

To summarize, we have presented MD simulation results of the structure and thermal boundary conductance of the wurtzite GaN/AlN (0001) interface using three different empirical interatomic potentials: the Stillinger–Weber (SW) potential developed by Zhou *et al.*, ¹⁹ the mixing rule-based Tersoff potentials, ^{20,21} and the transferrable Tersoff potential developed by Karaaslan *et al.* ²² Simulations with the different potentials all have produced similar misfit dislocation network and dislocation core structures. Although different interatomic potentials lead to quantitatively different dislocation properties and thermal boundary conductance values, all have produced the same dislocation network and core structure and have demonstrated a significant effect of misfit dislocations on the thermal conductance of the wurtzite GaN/AlN (0001) interface. Major results that are reproduced consistently by all three potentials are summarized as follows:

- (1) The misfit dislocation network at the wurtzite GaN/AlN (0001) interface consists of pure edge dislocations with a Burgers vector of $1/3\langle 1\bar{2}10\rangle$. The dislocations form a hexagonal-shaped network. The GaN unit cells near the interface undergo larger deformation than the AlN unit cells.
- (2) The GaN/AlN misfit dislocation core has an eight-atom ring structure, which is similar to the dislocation core structure found in the GaN single crystal.
- (3) By comparing the thermal boundary conductance of semicoherent GaN/AlN interfaces with that of coherent interfaces, the thermal boundary conductance of the semi-coherent interface is shown to be much smaller than that of the coherent interface. The misfit dislocations reduce the thermal boundary conductance by 47.1%, 21.9%, and 40.1% in the simulation with the SW potential, the mixing rule-based Tersoff potentials, and the transferrable Tersoff potential, respectively.
- (4) The thermal boundary conductance is found to increase with temperature significantly for both coherent and semi-coherent interfaces. It also increases with the length of the specimen. In addition, simulation results with different applied heat fluxes show that thermal boundary conductance is approximately a constant at different background temperatures.

We would like to note that the wurtzite GaN/AlN (0001) heterostructure studied in this work has an atomically flat interface, with misfit dislocations being the major defects in the heterostructure and without threading dislocations or stacking faults in the GaN or AlN layers. For heteroepitaxially grown GaN/AlN heterostructures, there are concurrent misfit and threading dislocations, and there is coupling between misfit dislocations at the interface and threading dislocations in the epilayer(s). Consequently, the thermal boundary conductance of the interface in such heterostructure can be expected to be further smaller and the size effect is then likely more pronounced due to possibly coupled, three-dimensional dislocation structures that consist both misfit and threading dislocations. To obtain such defect structures, we will need to simulate the kinetic processes of heteroepitaxial growth, which will be our future work.

ACKNOWLEDGMENTS

This material is based on research supported by the U.S. National Science Foundation under Award No. CMMI-1761512. The computer simulations are funded by the Extreme Science and Engineering Discovery Environment (XSEDE) under Allocation No. TG-DMR190008.

DATA AVAILABILITY

The data that support the findings of this study are available from the corresponding author upon reasonable request.

REFERENCES

- ¹H. Kroemer, Rev. Mod. Phys. 73, 783 (2001).
- ²J. Matthews and A. Blakeslee, J. Cryst. Growth 27, 118 (1974).
- ³S. M. Hu, J. Appl. Phys. **69**, 7901 (1991).
- ⁴A. E. Romanov, W. Pompe, G. Beltz, and J. S. Speck, Phys. Status Solidi B 198, 599 (1996).
- ⁵J. Arokiaraj, C. K. Leong, V. Lixian, A. M. Yong, and W. Xincai, Appl. Phys. Lett. **92**, 124105 (2008).
- ⁶J. Lee, R. F. Davis, and R J. Nemanich, Int. J. High Speed Electron. Syst. 14, 83 (2004).
- ⁷F. Mu, Z. Cheng, J. Shi, S. Shin, B. Xu, J. Shiomi, S. Graham, and T. Suga, ACS Appl. Mater. Interfaces 11, 33428 (2019).
- ⁸F. Mu, Y. Wang, R. He, and T. Suga, Materialia 3, 12 (2018).
- ⁹J. Jasinski, Z. Liliental-Weber, S. Estrada, and E. Hu, Appl. Phys. Lett. **81**, 3152 (2002).
- 10T. Suga and F. Mu, "Direct bonding of GaN to diamond substrate at room temperature," in 2020 IEEE 70th Electronic Components and Technology Conference (ECTC) (IEEE, 2020), p. 1328.
- ¹¹Y.-Y. Wong, E. Y. Chang, T.-H. Yang, J.-R. Chang, J.-T. Ku, M. K. Hudait, W.-C. Chou, M. Chen, and K.-L. Lin, J. Electrochem. Soc. 157, H746 (2010).
- 12 T. Jiang, Z. Wang, X. Ruan, and Y. Zhu, 2D Mater. 6, 015026 (2019).
- ¹³R. M. Radway, M.S. thesis, Massachusetts Institute of Technology, 2017.
- ¹⁴Y. Li, A. Bhattacharyya, C. Thomidis, Y. Liao, T. D. Moustakas, and R. Paiella, J. Appl. Phys. **104**, 083101 (2008).
- ¹⁵R. J. Kaplar, A. A. Allerman, A. M. Armstrong, M. H. Crawford, J. R. Dickerson, A. J. Fischer, A. G. Baca, and E. A. Douglas, ECS J. Solid State Sci. Technol. 6, O3061 (2017).
- ¹⁶H. Machhadani, P. Kandaswamy, S. Sakr, A. Vardi, A. Wirtmüller, L. Nevou, F. Guillot, G. Pozzovivo, M. Tchernycheva, A. Lupu, L. Vivien, P. Crozat, E. Warde, C. Bougerol, S. Schacham, G. Strasser, G. Bahir, E. Monroy, and F. H. Julien, New J. Phys. 11, 125023 (2009).
- 17C. A. Polanco and L. Lindsay, Phys. Rev. B 99, 075202 (2019).
- ¹⁸A. van Roekeghem, B. Vermeersch, J. Carrete, and N. Mingo, Phys. Rev. Appl. 11, 034036 (2019).
- ¹⁹X. W. Zhou, R. E. Jones, C. J. Kimmer, J. C. Duda, and P. E. Hopkins, Phys. Rev. B 87, 094303 (2013).
- ²⁰M. Tungare, Y. Shi, N. Tripathi, P. Suvarna, and F. S. Shahedipour-Sandvik, Phys. Status Solidi A 208, 1569 (2011).
- ²¹j. Nord, K. Albe, P. Erhart, and K. Nordlund, J. Phys.: Condens. Matter 15, 5649 (2003).
- 22Y. Karaaslan, H. Yapicioglu, and C. Sevik, Phys. Rev. Appl. 13, 034027 (2020).
- ²³ A. Béré and A. Serra, Phys. Rev. B **65**, 205323 (2002).
- ²⁴P. Ruterana, B. Barbaray, A. Béré, P. Vermaut, A. Hairie, E. Paumier, G. Nouet, A. Salvador, A. Botchkarev, and H. Morkoç, Phys. Rev. B 59, 15917 (1999).
- 25X. W. Zhou, R. E. Jones, J. C. Duda, and P. E. Hopkins, Phys. Chem. Chem. Phys. 15, 11078 (2013).
- ²⁶L. Zhang, H. Yan, G. Zhu, S. Liu, Z. Gan, and Z. Zhang, Crystals 8, 279 (2018).

- 27H. Li, H. Xiang, H. Huang, Z. Zeng, and X. Peng, Ceram. Int. 46, 11556
- ²⁸J. Tersoff, Phys. Rev. B **39**, 5566 (1989).
- ²⁹J. Kioseoglou, E. Kalesaki, L. Lymperakis, G. P. Dimitrakopulos, P. Komninou, and T. Karakostas, Phys. Status Solidi A 206, 1892 (2009).
- 30 P. K. Schelling, S. R. Phillpot, and P. Keblinski, Phys. Rev. B 65, 144306 (2002). ³¹A. Stukowski and K. Albe, Modell. Simul. Mater. Sci. Eng. **18**, 085001 (2010).
- ³²A. Stukowski, Modell. Simul. Mater. Sci. Eng. **18**, 015012 (2010).
- 33I. Yonenaga, MRS Internet J. Nitride Semicond. Res. 7, e6 (2002).
- 34A. K. Kandalam, R. Pandey, M. A. Blanco, A. Costales, J. M. Recio, and J. M. Newsam, J. Phys. Chem. B **104**, 4361 (2000).

 35K. Termentzidis, M. Isaiev, A. Salnikova, I. Belabbas, D. Lacroix, and
- J. Kioseoglou, Phys. Chem. Chem. Phys. 20, 5159 (2018).
 36 H. Yoo, S. Yoon, K. Chung, S.-H. Kang, Y.-K. Kwon, G.-C. Yi, and M. Kim,
- Appl. Phys. Lett. 112, 131901 (2018).

 37B. M. Garraway and K.-A. Suominen, Rep. Prog. Phys. 58, 365 (1995).
- 38 P. K. Schelling, S. R. Phillpot, and P. Keblinski, Appl. Phys. Lett. 80, 2484 (2002). **39**E. S. Landry and A. J. H. McGaughey, Phys. Rev. B **80**, 165304 (2009).